



# 3D printable electroconductive gelatin-hyaluronic acid materials containing polypyrrole nanoparticles for electroactive tissue engineering

Aleksandra Serafin<sup>1</sup> · Mario Culebras<sup>2</sup> · J. Miguel Oliveira<sup>3,4</sup> · Jacob Koffler<sup>5,6</sup> · Maurice N. Collins<sup>1,7</sup>

Received: 27 December 2022 / Revised: 29 March 2023 / Accepted: 3 April 2023 / Published online: 20 May 2023  
© The Author(s) 2023

## Abstract

Electrically conductive bio-scaffolds are explored in the field of tissue engineering (TE) as a solution to address the clinical need of electroactive tissues, finding applications in nervous, cardiac, and spinal cord injury repair. In this work, we synthesise polypyrrole nanoparticles (PPy NP) via the mini-emulsion method with further combination with a gelatin/hyaluronic acid (HA) hydrogel to create electroconductive Gel:HA:PPy-NP TE scaffolds. Electroconductive Gel:HA:PPy-NP scaffolds possess excellent mechanical properties at  $1.08 \pm 0.26$  MPa, closely matching the reported mechanical performance of the spinal cord. Scaffolds were designed with controlled porosity of  $526.2 \pm 74.6$ – $403.9 \pm 57.4$   $\mu\text{m}$ , and conductivities of  $4.3 \times 10^{-6} \pm 1.1 \times 10^{-6}$   $\text{S}\cdot\text{cm}^{-1}$  were reached. Rheological studies show that prior to lyophilisation, the Gel:HA:PPy-NP hydrogels display a shear-thinning behaviour. These gels were subsequently 3D printed into predefined 2 layer lattice geometries and displayed excellent post-printing shape fidelity. In vitro studies show that the Gel:HA:PPy-NP scaffolds are cytocompatible with mesenchymal stem cells and neuronal stem cells and display encouraging cell attachment and proliferation profiles. Based on these results, the incorporation of PPy NPs into Gel:HA biomaterial scaffolds enhances the conductive capabilities of the material, while showcasing biocompatible behaviour with cell cultures. Hence, Gel:HA:PPy-NP scaffolds are a promising TE option for stimulating regeneration following nervous tissue injury.

**Keywords** Electroconductive scaffolds · PPy nanoparticles · Tissue engineering · Neural repair · 3D printing

## 1 Introduction

Tissue engineering (TE), and particularly TE scaffolds, are under intensive research amongst the biomedical community to combat worldwide shortages of available tissues and organs for transplantation purposes [1]. Tissue engineering scaffolds can be developed using a myriad of biomaterials, although they can be summarised in two distinct categories:

natural and synthetic biomaterials. Synthetic polymers include polylactic acid (PLA) [2] or polycaprolactone (PCL) [3]. These materials offer mechanically robust scaffolds; however, concerns such as long degradation times, residual toxic monomers arising from incomplete polymerisations, as well as structural and mechanical instability, can render them unsuitable for applications such as neuronal TE [4, 5].

Natural materials such as hyaluronic acid or gelatin offer the potential for biomimicry with the control of the

✉ Jacob Koffler  
ykoffler@ucsd.edu

✉ Maurice N. Collins  
maurice.collins@ul.ie

<sup>1</sup> School of Engineering, Bernal Institute, University of Limerick, Limerick, Ireland

<sup>2</sup> Materials Science Institute (ICMUV), Universitat de València, c/Catedrático, José, Beltrán 2, Paterna, Valencia 46980, Spain

<sup>3</sup> 3B's Research Group, I3Bs—Research Institute on Biomaterials, Biodegradables and Biomimetics Headquarters of the European Institute

of Excellence On Tissue Engineering and Regenerative Medicine, AvePark, Parque de Ciência E Tecnologia, University of Minho, Zona Industrial da Gandra, Barco, Guimarães 4805-017, Portugal

<sup>4</sup> ICVS/3B's—PT Government Associate Laboratory, Braga, Braga 4710-057, Portugal

<sup>5</sup> Department of Neuroscience, University of California San Diego, La Jolla, CA 92093, USA

<sup>6</sup> Veterans Affairs Medical Center, San Diego, CA, USA

<sup>7</sup> Health Research Institute and AMBER, University of Limerick, Limerick V94 T9PX, Ireland

immunomodulatory response of the host tissue. The inclusion of collagen or gelatin provides cellular attachment sites by means of arginine–glycine–aspartic acid (RGD) and GFOGER peptide sequences similar to the extracellular matrix of tissues [6, 7]. Hyaluronic acid (HA) has also been extensively used to modulate the host tissue response, for example, by means of CD44 and HA-mediated motility (RHAMM) receptors [8–10]. For example, in a spinal cord injury, axon regeneration is very limited due to the hostile and inhibitory local environment around the injury site [11, 12]. To overcome the limited tissue healing ability in SCI, TE scaffolds, and conduits offer an environment for homing cells and supporting regenerating neural tissues [13, 14]. High molecular weight HA (HMWHA) has been shown to decrease pro-inflammatory astrocyte reactivity in traumas of the central nervous system, while low molecular weight HA (LMWHA) induces astrocyte proliferation and increases pro-inflammatory responses [15, 16].

The development of TE scaffolds has also been widely explored in 3D printing scenarios, primarily due to the advantage in controlling the architecture of the scaffold to a high degree when compared to traditional moulding techniques [6, 17, 18]. The choice as to the printing material is also greatly important, as the necessary parameters such as shear thinning behaviour, as well as post-printing shape fidelity maintenance, must be maintained for a successful scaffold 3D print to be obtained [19–21]. The incorporation of capacitors and piezoelectric elements into 3D printing strategies has also been explored [22–24], though in terms of TE strategies, a shift towards 3D printing conductive biomaterial scaffolds has been observed to date. Cells are known to be influenced by electrical stimulation [14, 25], especially if they are of a conductive nature such as cardiac [26], muscle [27], spinal or nerve cells [25, 28]. Raising the conductivity of scaffolds can be achieved in various ways, including through carbon-based additives such as graphene oxide, carbon nanofibers and carbon nanotubes [6], or by utilising conductive polymers such as polyaniline and poly(3,4-ethylenedioxythiophene) polystyrene sulfonate (PEDOT:PSS) [29, 30]. Although the utilisation of these additives has shown some promising results, the drawbacks of low conductivity in neutral pH, insolubility in water, potential toxicity issues due to PSS, poor bio-functionality and/or biocompatibility have severely limited their successful use in *in vivo* applications [31–33].

Polypyrrole (PPy) is another widely known electrically conductive polymer utilized due to its biocompatibility and minimal immune response, with the PPy often combined with biomaterials via *in situ* polymerisation [34, 35]. However, several limitations of PPy must be addressed, namely, instability and molecular damage in biological aqueous environments due to the dissolved oxygen, low cellular adhesion, poor water processability and insolubility, and post-synthesis processing difficulties resulting in poor mechanical properties

[36, 37]. These limitations have restricted the successful incorporation of PPy in hydrogel systems and its application in TE scaffolds.

In this study, PPy nanoparticles (NPs) were synthesised to overcome the outlined limitations by utilising chemical oxidation polymerization. The mini-emulsion method was used to ultrasonically mix the disperse and continuous phase, consisting of pyrrole as the monomer and poly(diallyldimethylammonium) chloride (PDADMAC) as a surfactant. The presence of the surfactant stabilises the nanodroplets, which then act as nanoreactors with the addition of iron(III) *p*-toluenesulfonate hexahydrate. The study of PPy NPs in combination with biomaterials has been limited to date [38, 39].

The PPy NPs offer a new route to increase the conductivity of a more varied range of biomaterial components than the traditionally used PPy while maintaining cellular attachment and proliferation. The PPy NPs also offer the possibility for further functionalisation of their surface chemistry to allow, for example, drug incorporation by altering the surfactant used during the NP synthesis. The PPy NPs were combined with gelatin and HMWHA to develop Gel:HA:PPy-NP scaffolds. These biomaterials were chosen as they provide strong cellular attachment and immunomodulatory properties [7, 8, 15, 40]. The scaffolds were fully characterised by means of mechanical, morphological, chemical and biocompatibility responses. The materials were also successfully 3D printed into predetermined shapes, showing excellent shape fidelity characteristics. The strategy of combining printable immunomodulatory biomaterials with conductive NP additives shows promise for a wide range of electrically conductive tissue repair strategies and geometries.

## 2 Materials and methods

### 2.1 Materials

For the synthesis of the PPy NPs, poly(diallyldimethylammonium chloride) solution (PDADMAC) 20 wt% in H<sub>2</sub>O<sub>2</sub>, pyrrole, Iron(III) *p*-toluenesulfonate hexahydrate (Fe-Tos) and H<sub>2</sub>O<sub>2</sub> (30 wt%) were all purchased from Sigma-Aldrich (Ireland).

For the development of the Gel:HA:PPy-NP scaffolds, gelatin (300 Bloom, Type A), N-(3-dimethylaminopropyl)-N'-ethylcarbodiimide hydrochloride (EDC), N-hydroxysuccinimide (NHS) and phosphate-buffered saline (PBS) were all purchased from Sigma-Aldrich (Ireland). Hyaluronic acid (1.8 MDa molecular weight) was purchased from Shanghai Easier Industrial Development (China).

For cell culture experiments, the minimum essential medium alpha (MEM $\alpha$ ), foetal bovine serum GlutaMAX, Penicillin–Streptomycin, DAPI and propidium iodine were

all purchased from Sigma Aldrich (USA). Alamar Blue™, Vybrant DiI Cell-Labeling Solution and Calcein AM were all purchased from Invitrogen (ThermoFisher, USA). ENStem-A™ Neural Expansion Medium, L-Glutamine and FGF-2 were all purchased from EDM Millipore (USA).

## 2.2 Synthesis of polypyrrole nanoparticles (PPy NPs)

The synthesis of the PPy NPs was conducted by chemical oxidation polymerization in mini-emulsion, as shown in Fig. S2a, modified from [41]. In summary, 0.037 M (200  $\mu$ L) of pyrrole was added into an aqueous solution of PDAD-MAC in water (40 mL). The solution was stirred at 800 RPM for 5 min followed by tip ultrasonication (Soniprep 150 Plus, MSE, UK) for 10 min over ice at an amplitude of 20  $\mu$ m to obtain a mini-emulsion. 0.056 M of Fe-Tos solution in DI water (10 mL) was added dropwise to the mini-emulsion under constant stirring at 45 °C. 0.001 M of H<sub>2</sub>O<sub>2</sub> was then added and the reaction was left to run overnight. The NP purification was then conducted by means of centrifugation at 8700 RPM for 20 min. The supernatant was discarded, and the purification step repeated three times, with a final redispersion in 40 mL of DI water.

## 2.3 Preparation of gelatin/hyaluronic acid/PEDOT NPs lyophilised scaffolds

Gel:HA:PPy-NP hydrogel solution was prepared by adding 10% w/v of gelatin to the PPy NP solution at 50 °C. The PPy NP solution was diluted into 1 $\times$ , 0.5 $\times$  and 0.25 $\times$  concentrations before the addition of gelatin, as shown in Table 1. The solution was stirred until fully dissolved, followed by the addition of 1% w/v of HA and cast into moulds, 13.5 mm in diameter and 4 mm high. The solution was then slowly frozen at -20 °C for 2 h, followed by freezing at -80 °C overnight. Lyophilisation of the hydrogels to create Gel:HA:PPy-NP scaffolds was conducted with Eurotherm LS40/60 (Severn Science Ltd, Bristol, England) with cooling for 8 h at -30 °C at 100 mbar, first drying for 16 h at -10 °C under 0.1 mbar and secondary drying for 2 h at 20 °C (under vacuum). The lyophilised scaffolds

**Table 1** Composition of the prepared Gel:HA:PPy-NP scaffolds

| Sample name                 | PPy concentration (mg/ml) | Gelatin (% w/v) | Hyaluronic acid (% w/v) |
|-----------------------------|---------------------------|-----------------|-------------------------|
| Gel:HA:PPy-NP 1 $\times$    | 2.1                       | 10              | 1                       |
| Gel:HA:PPy-NP 0.5 $\times$  | 1.05                      | 10              | 1                       |
| Gel:HA:PPy-NP 0.25 $\times$ | 0.525                     | 10              | 1                       |
| Gel:HA Control              | 0                         | 10              | 1                       |

were then removed from the circular moulds and crosslinked with EDC:NHS, 50 mM:10 mM respectively, in 1 $\times$  PBS solution at 4 °C for 24 h before washing trice in DI water. Control samples were synthesised in a similar manner, using DI water instead of NP solution. The scaffold preparation schematic is shown in Fig. S2.

## 2.4 Characterisation of Gel:HA:PPy-NP scaffolds

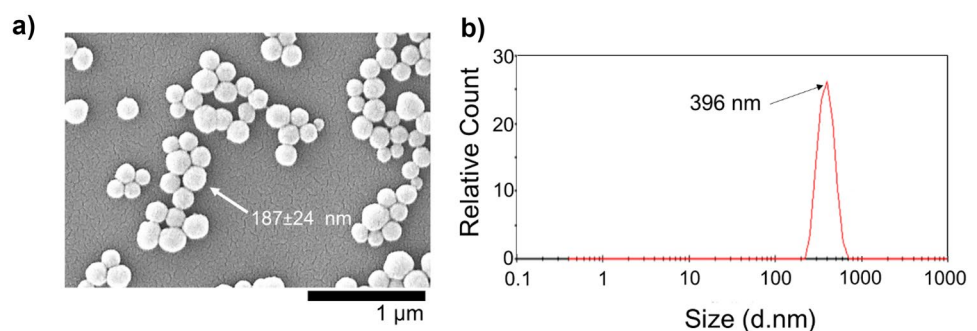
Scanning electron microscope (SEM) analysis of PPy NPs was conducted by means of Hitachi SU70 SEM. The PPy NPs solution was deposited onto a glass slide, and the water was allowed to evaporate. The lyophilised Gel:HA:PPy-NP scaffolds were sputtered with gold prior to SEM imaging. An imaging voltage of 10 kV was used to visualise both the NPs and the Gel:HA:PPy-NP scaffolds.

Dynamic light scattering (DLS) analysis of the PPy NPs was also conducted using a particle size analyser (Zetasizer Nano ZS, Malvern Instruments, Malvern, UK). The NPs were diluted to a of low concentration in a 0.3 M KCl aqueous solution.

The compressive behaviour of the Gel:HA:PPy-NP scaffolds was tested using an in-house compression testing facility equipped with a 1 kN load cell and a compression rate of 1 mm/s<sup>-1</sup> between parallel plates. The slope in the linear region of a normalised stress vs. strain graph was used to calculate Young's Modulus.

The resistivity of the Gel:HA:PPy-NP scaffolds was measured with an Ohm meter using the two-probe method. The conductivity of the samples was then calculated by means of Pouillet's Law as shown in Eq. 1.

**Fig. 1** a SEM analysis of synthesised PPy NPs. b DLS measurement of PPy NPs in the hydrodynamic state.



$$\sigma = \frac{l}{RA} \quad (1)$$

where  $\sigma$  is the conductivity,  $l$  is the sample length,  $A$  is the cross-sectional area, and  $R$  is the resistance.

Fourier-transform infrared spectroscopy (FTIR) spectra of Gel:HA:PPy-NP scaffolds in the range 500–4000  $\text{cm}^{-1}$  for 10 scans was conducted with spectrum 100 FTIR (PerkinElmer, USA).

The swelling profiles of the Gel:HA:PPy-NP scaffolds were tested by firstly drying out the samples in a vacuum oven overnight. Subsequently, the dry mass of the samples was weighed prior to rehydration in PBS at 37 °C for a period of 96 h. At specified time points, the wet mass of samples was re-taken, and the swelling degree (SD) was calculated using Eq. 2.

$$SD(\%) = \left( \frac{W_s - W_d}{W_d} \right) * 100\% \quad (2)$$

where  $W_s$  is the hydrogel swollen mass, and  $W_d$  is the dried mass.

The rheological behaviour of the Gel:HA:PPy-NP hydrogel (before the lyophilisation step) was investigated using a hybrid rheometer (TA Instruments, USA), with the techniques described in [6]. In brief, disposable 25 mm aluminum rheological plates with a measurement gap of 550  $\mu\text{m}$  were used during the analysis. The hydrogel samples were tested using the following testing parameters: (1) frequency sweep from 0.1 to 100 rad/s at the determined constant strain of 2% and (2) steady-state flow test with shear rates ranging from 0.5 to 500  $\text{s}^{-1}$  and 3) recovery test under shear rates of 0.1  $\text{s}^{-1}$  and 100  $\text{s}^{-1}$ . All the experiments were conducted at 37 °C.

## 2.5 3D Printing of Gel:HA:PPy-NP

3D Printing capabilities of Gel:HA:PPy-NP hydrogels were studied with an Allevi 2 Printer (Allevi, USA). 3D lattice models were created using CAD software (SolidWorks 2016) and spliced into a printable design via a splicing software (Repetier-Host) prior to 3D printing. Printed designs were constructed as 10 mm in width square lattices with two layers printed. Gel:HA:PPy-NP hydrogel lattices were printed using a printing speed of 6  $\text{mm}\cdot\text{s}^{-1}$ . The pressure and temperature parameters inside the printing cylinder were kept between 4–6 PSI and at 31–33 °C, respectively.

## 2.6 In vitro cytocompatibility assessment of Gel:HA:PPy-NP NP scaffolds

Gel:HA:PPy-NP scaffolds were initially tested for potential cytotoxicity by means of Alamar Blue™ Proliferation Assay. The mesenchymal stem cells (MSCs) were seeded

at a density of  $0.2 \times 10^6$  cells/scaffold onto pre-conditioned Gel:HA:PPy-NP scaffolds in a 24-well plate and supplemented with 1 mL of cell culture media with overnight incubation. The Alamar Blue™ protocol was used following the manufacturer's protocol as described.

Biocompatibility of the Gel:HA:PPy-NP scaffolds was assessed by means of LIVE/DEAD staining with Calcein AM and propidium iodine. The MSCs were seeded at a density of  $0.2 \times 10^6$  cells/scaffold onto pre-conditioned Gel:HA:PPy-NP scaffolds in a 24-well plate and cultured for a period of 96 h. Cells were imaged by means of Carl Zeiss Microscope (USA) for fluorescence imaging. Quantitative analysis of the cell viability was completed using the ImageJ software.

Visualisation of the MSCs and tdTomato Neuronal Stem Cells (NSCs) morphology and cell attachment was also conducted. MSCs and NSCs previously stained with Vybrant DiI (1:200) were seeded at a density of  $0.1 \times 10^6$ – $0.25 \times 10^6$  cells per scaffold onto pre-conditioned Gel:HA:PPy-NP scaffolds in a 24-well plate. After a period of 96 h, the cells were fixed with 4% paraformaldehyde (PFA), stained with DAPI (1:1000), and imaged. Detailed outlines of the in vitro testing can be found in the Supplementary Information. The schematic of in vitro biocompatibility testing of cells seeded on conductive scaffolds is shown in Fig. S1.

## 2.7 Statistical analysis

Experiments were conducted in triplicates, with the data presented as mean  $\pm$  standard deviation. To determine the statistical significance, one-way analysis of variance (ANOVA) was employed with the  $p$  value of  $< 0.05$  considered as statistically significant ( $*p < 0.05$ ). A two-way ANOVA was employed for the Alamar Blue™ cytocompatibility analysis, with the  $p$  value of  $< 0.05$  considered as statistically significant ( $*p < 0.05$ ).

## 3 Results and discussion

### 3.1 Morphological characterisation of PPy NPs and Gel:HA:PPy-NP scaffolds

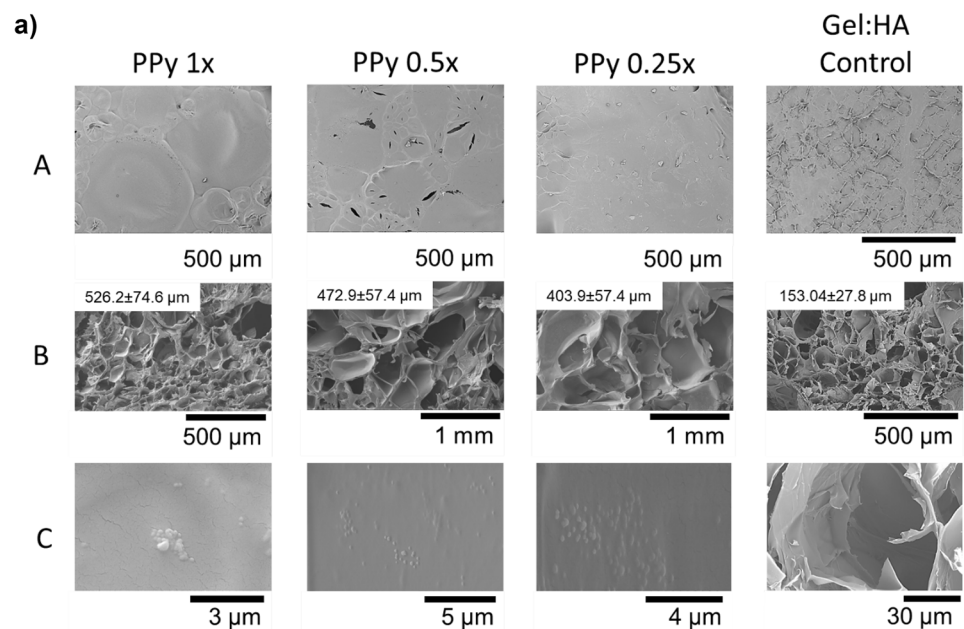
Polypyrrole nanoparticles were successfully synthesised using the mini-emulsion method as shown in Fig. S2a. Morphological analysis of the PPy NPs shows that the NPs possess a rounded and uniform morphology, with an average diameter of  $187 \pm 24$  nm, as indicated by ImageJ analysis of the SEM image, with an example shown in Fig. 1a. Nanoparticle analysis via a DLS technique shows that in their hydrated state, the PPy NPs had a hydrodynamic size

of 396 nm, as shown in Fig. 1b. The variability in the reported NP sizes can be attributed to swelling and aggregation factors present in hydrodynamic values.

Incorporation of the PPy NPs into the Gel:HA blended solutions (Fig. S2b) created a black viscous solution, with an increase in the viscosity observed in part due to the high MW of the HA. After lyophilisation, the Gel:HA:PPy-NP scaffolds were examined via SEM to determine their internal architecture, as shown in Fig. 2a. The Gel:HA:PPy-NP scaffolds show a well-defined internal porosity across all samples with the pore size ranging from  $526.2 \pm 74.6$ – $403.9 \pm 57.4$   $\mu\text{m}$ . The pore size was measured by image analysis using ImageJ as shown in Fig. S2b. The Gel:HA control had an average pore size of  $153.04 \pm 27.8$   $\mu\text{m}$ , though no significant difference between the PPy NPs scaffold groups was found. The porosity of the scaffolds is attributed to the manufacturing

protocol with slow freezing of the samples prior to lyophilisation. Slow freezing allows for larger ice crystals to form within the scaffold, which are then removed during lyophilisation, leaving a porous geometry throughout the scaffolds [42]. The addition of the PPy NPs, which are hydrophilic, contributes to increased pore size in the PPy NPs scaffolds when compared to that of the Gel:HA control. The presence of the NPs in the material may lead to slower heat dissipation and thus a slower freezing process due to the formation of ice bulges within the hydrogel. This in turn influences the morphological architecture and porosity of the scaffold [43, 44]. Overall, porosity in the range of 100–500  $\mu\text{m}$  has been shown to support cellular interactions by allowing adequate oxygen and nutrient diffusion, particularly for MSCs [40, 45]. Additionally, the pore size of the scaffolds can be easily tailored by the processing conditions.

**Fig. 2** a SEM Analysis of the porosity and PPy NP distribution within Gel:HA:PPy-NP scaffolds. **A** Surface view of Gel:HA:PPy-NPs scaffolds. **B** Internal porosity of the Gel:HA:PPy-NPs scaffolds, with average pore diameter. **C** Magnification of PPy NPs on the internal surfaces of the Gel:HA:PPy-NPs scaffolds. **b** Internal pore diameter of Gel:HA:PPy-NP scaffolds. (\* $p < 0.05$  ( $n = 3$ , mean  $\pm$  SD) is indicated where statistical difference is observed)



Additionally, the distribution of the PPy NPs across all samples was homogeneous with no aggregation of NPs observed, as shown in Fig. 2(a-C). This is difficult to achieve in viscous systems such as the Gel:HA:PPy-NP hydrogels.

### 3.2 Mechanical characterisation of Gel:HA:PPy-NP scaffolds

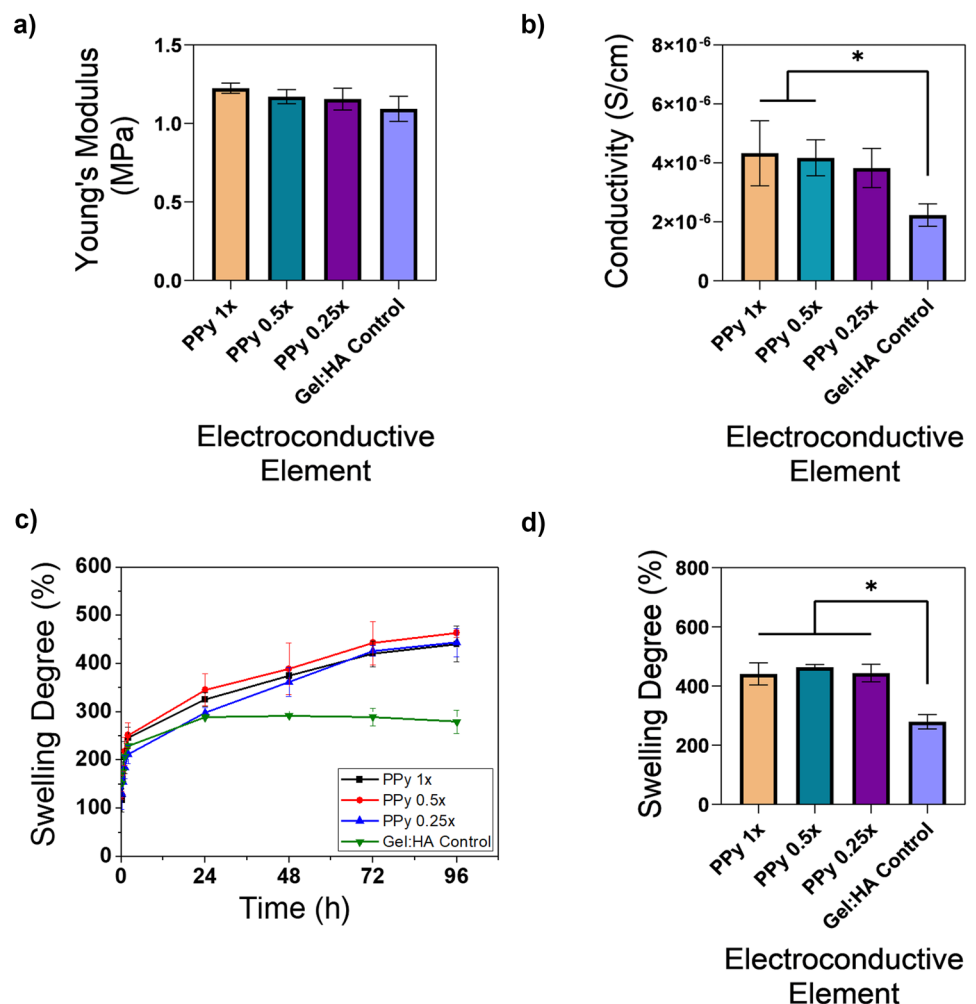
The mechanical properties of Gel:HA:PPy-NP scaffolds were investigated using a compression testing facility, with the results shown in Fig. 3a. Increasing the concentration of the PPy NPs increased the Young's Modulus from  $1.16 \pm 0.07$  MPa for the PPy 0.25x scaffold to  $1.2 \pm 0.3$  MPa for the PPy 1x scaffold. All PPy NP scaffold samples had a higher Young's Modulus than the control at  $1.09 \pm 0.08$  MPa, though no significant difference was observed between the samples. The mechanical properties of materials for TE strategies are one of the important factors to consider when designing a scaffold for specific purposes and should ideally match the mechanical response of the native host tissue.

Taking spinal cord injury repair as an example, the human spine is generally regarded to possess a Young's Modulus of 0.8–1.37 MPa, with the PPy NP scaffolds matching this mechanical behaviour closely [15, 46, 47].

### 3.3 Conductive characterisation of Gel:HA:PPy-NP scaffolds

The resistance of the scaffolds was measured using a 2 probe method and was converted into conductivity using Pouille's law, with the results shown in Fig. 3b. The addition of the NPs increased the conductivity almost two-fold when compared to the Gel:HA control. The conductivity of the PPy 1x sample was  $4.3 \times 10^{-6} \pm 1.1 \times 10^{-6}$  S.cm<sup>-1</sup> when compared to the Gel:HA control at  $2.3 \times 10^{-6} \pm 4 \times 10^{-7}$  S.cm<sup>-1</sup>, matching the values of other electroconductive scaffolds which have shown to induce improved cellular function [48]. The differences in the conductivity between the PPy NP scaffold concentrations were not significant due to the small quantities of the added NPs when compared to the overall scaffold formulation. It is hypothesised that the percolation

**Fig. 3** **a** Young's Modulus of Gel:HA:PPy-NPs scaffolds. **b** Conductivity of the Gel:HA:PPy-NP scaffolds. **c** Swelling profiles of the Gel:HA:PPy-NP scaffolds. **d** Swelling degree at 96 h of observation. (\* $p < 0.05$ , ( $n = 3$ , mean  $\pm$  SD) is indicated where statistical difference is observed)



threshold has not been reached with the specified NP concentrations, therefore the addition of higher concentrations of PPy NPs would increase the conductivity once this threshold is reached. It is inferred that the interactions between the NPs and the ionic conductive component of the water in the hydrated scaffold were the significant driving factors for the increase in the conductivity with the specified NP concentrations. It should be noted that conductivity in cellular interactions is primarily driven by ionic exchange, and not electron transfer. Therefore, the conductivity of an electroconductive TE material should aim to incorporate both electronic and ionic conductivity contributions to bridge the gap between the electrical scaffold and host tissue conductive behaviours [49].

### 3.4 Swelling properties of Gel:HA:PPy-NP scaffolds

Determination of the swelling properties and crosslinking effectiveness of the developed materials was conducted on the Gel:HA:PPy-NP hydrogel scaffolds by means of swelling studies, and the results are presented in Fig. 3c. The swelling degree initially increased for all samples during the first 24 h. Swelling profiles for PPy NP-loaded scaffolds were very similar over the 96 h observational period, with the swelling degree increasing gradually over time. Conversely, the swelling degree of the Gel:HA reached equilibrium after 24 h. At the 96 h timepoint, shown in Fig. 3d, the swelling degree of the PPy 1 × scaffolds was significantly higher at  $440 \pm 37\%$  than the Gel:HA control at  $279 \pm 24\%$ . It may be speculated that the addition of the hydrophilic PPy NPs into the Gel:HA system improves the water uptake of the scaffolds due to the positive surface charges of the NP and the PDADMAC used in their synthesis [50]. While PDADMAC is known to possess a high affinity for water uptake [50, 51], this could increase the overall hydrophilic character of the PPy NP scaffolds and establish a higher swelling degree when compared to the control, as the swelling degree of polyampholytic polymers such as gelatin depends on charge distribution, amongst other factors [52].

It is well established that EDC activates carboxyl groups to crosslink with primary amino acids on adjacent gelatin chains, while the addition of the NHS stabilises the reaction and prevents molecular rearrangement [53, 54]. We speculate that crosslinking efficiency is disrupted in part due to the presence of the PPy NPs and the polyelectrolyte PDADMAC [55]. The NPs act as a filler within the Gel:HA polymer matrix, and therefore, their presence affects the

crosslinking efficiency between adjacent gelatin chains, resulting in higher swelling degrees [53, 54].

### 3.5 Chemical analysis of Gel:HA:PPy-NP scaffolds

Figure 4a shows a wide band at  $3300 \text{ cm}^{-1}$  associated with O–H and N–H stretching attributed to the presence of gelatin and HA in the scaffold composition [6, 41, 56]. Bands at  $3500\text{--}3200 \text{ cm}^{-1}$  and  $3070 \text{ cm}^{-1}$  are attributed to gelatin amide A and B, respectively [56]. The peak at  $1630 \text{ cm}^{-1}$  relates to gelatin amide I band, which represents the C–O and C–N stretching originating from the –NH group of the gelatin, while the amide II and III bands can be attributed to C–N stretching and N–H bending of the gelatin and these are attributed to the  $1545 \text{ cm}^{-1}$  and  $1235 \text{ cm}^{-1}$  peaks, respectively [6, 56].

Characteristic HA bands are observed at  $2930 \text{ cm}^{-1}$ ,  $1630 \text{ cm}^{-1}$ , and  $1030 \text{ cm}^{-1}$ , representing the C–H stretching vibration, amide carbonyl, and the presence of C–OH stretching, respectively [41, 56].

Distinctive PPy NP peaks are not clearly observed in the scaffold spectra due to the small volume of NPs added to the scaffolds when compared to the overall scaffold composition. Typical FTIR spectra for PPy NPs are shown in Fig. 4b. Bands at  $1547 \text{ cm}^{-1}$  and  $1468 \text{ cm}^{-1}$  relate to vibrations of the polypyrrole ring C=C stretching and C–N stretching, respectively. The peak at  $1165 \text{ cm}^{-1}$  is due to the C–N stretching vibrations, while the peaks at  $1295 \text{ cm}^{-1}$  and  $1035 \text{ cm}^{-1}$  are attributed C=C in-ring stretching and C–N deformation [57, 58].

### 3.6 Rheological analysis of Gel:HA:PPy-NP hydrogel

Rheological assessment of the Gel:HA:PPy-NP hydrogels are shown in Fig. 5a–d. The storage and loss moduli are presented in Fig. 5a–b. The addition of PPy NPs acted as a ‘filler’ to the overall hydrogel composition. Therefore, increasing the NP concentration increased the storage and loss modulus values, though all hydrogels are within their solid-elastic response, as shown by higher values of the storage modulus than loss modulus.

The hydrogels all display shear-thinning behavior, as shown in Fig. 5c. The addition of PPy NPs increases viscosity, for example, the viscosity of the Gel:HA sample decreases from  $15.9 \text{ Pa}\cdot\text{s}$  to  $1.5 \text{ Pa}\cdot\text{s}$  when the shear rate is increased from  $2$  to  $50 \text{ s}^{-1}$ , while the PPy 1 × sample viscosity decreases from  $282.6$  to  $11.2 \text{ Pa}\cdot\text{s}$  over the same shear rate range. Recovery profiles for the hydrogels are shown in Fig. 5d. This analysis simulates 3D printing conditions,

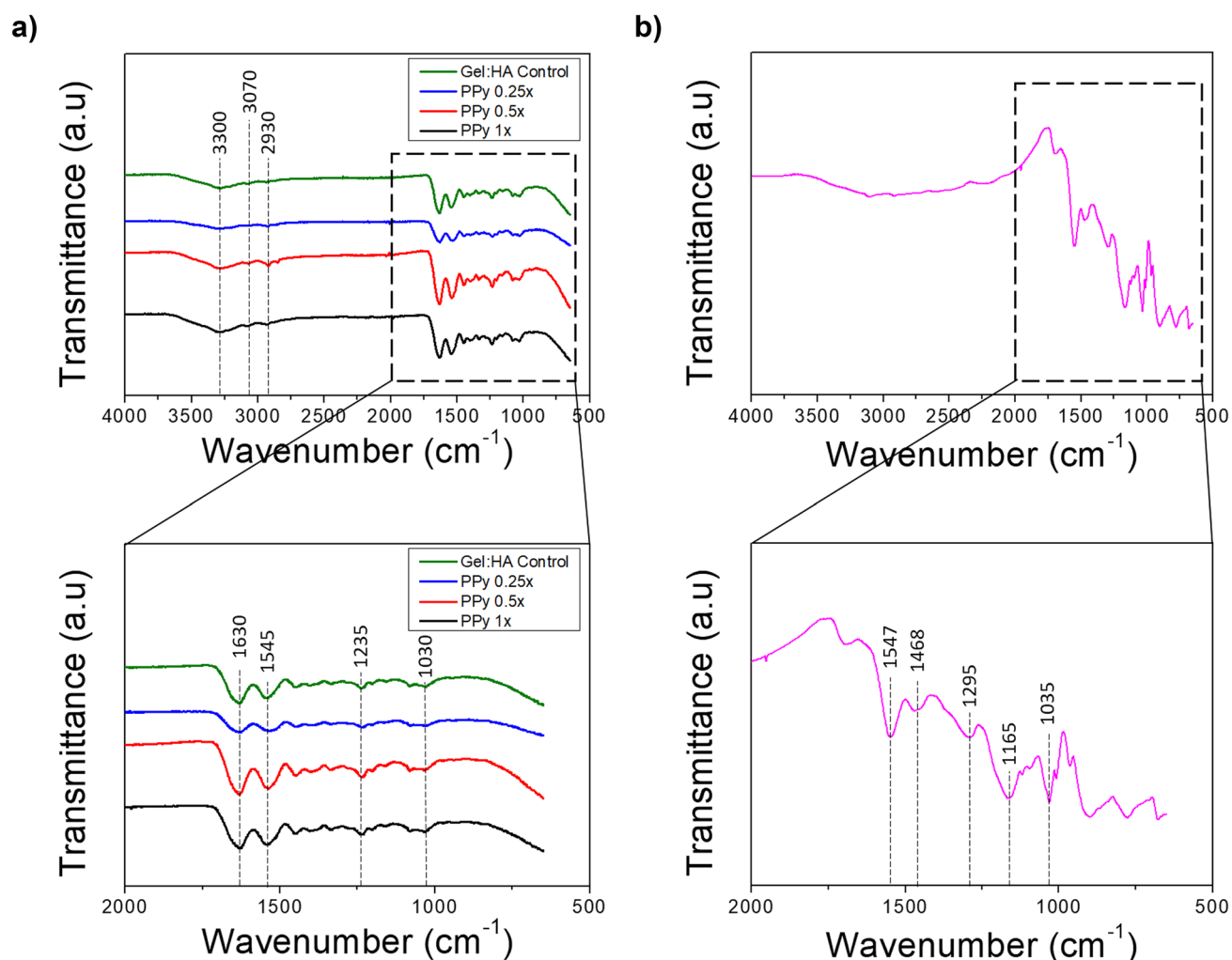


**Fig. 4** **a** FTIR spectra of Gel:HA:PPy-NPs scaffolds. **b** FTIR spectra of PPy NPs

with the initial low shear rate simulating the material in the printing cartridge. Increasing the shear rate to  $100 \text{ s}^{-1}$  simulates a higher shear experienced during extrusion through a narrow printing nozzle, with the shear rate decreasing drastically back down to a negligible  $0.1 \text{ s}^{-1}$  after the material is printed. The recovery of the material to higher viscosities following the printing step is crucial in maintaining shape fidelity post-printing. Once this is achieved, a post-printing crosslinking regime can be introduced. All hydrogels exhibited this recovery behaviour. For example, the PPy  $1 \times$  sample initially had a high viscosity of  $12,453 \text{ Pa}\cdot\text{s}$  which decreased to  $29.7 \text{ Pa}\cdot\text{s}$  upon application of higher shear rates. Interestingly, 5 s after removal of the high shear rate, the viscosity recovered to  $2020.14 \text{ Pa}\cdot\text{s}$  with a recovery rate of 16.2% of the initial viscosity. At the 10 s, 20 s, and 30 s time points the recovery rates measured at 21.8%, 27.9% and 31%, respectively. The re-organisation of the polymer network chains is not instantaneous [6, 59], though as the

majority of the PPy NP material recovery can be observed in the initial 5–10 s window, this augers well for its deployment as a bioink.

### 3.7 3D Printing of Gel:HA:PPy-NP hydrogels

Gel:HA:PPy-NP hydrogels with varying PPy NP loadings were utilised for 3D printing trials of 10-mm square lattices, comprising of 2 layers, with the results shown in Fig. 6. All samples, along with the control, were successfully 3D printed. Samples exhibited a defined post-printing shape fidelity, with good filament line spreading and height maintenance observed [60]. At room temperature, the lattices could be handled without the need for crosslinking. This showcases that the Gel:HA:PPy-NP material can be processed in a variety of methods to suit future scaffold geometry and application requirements.



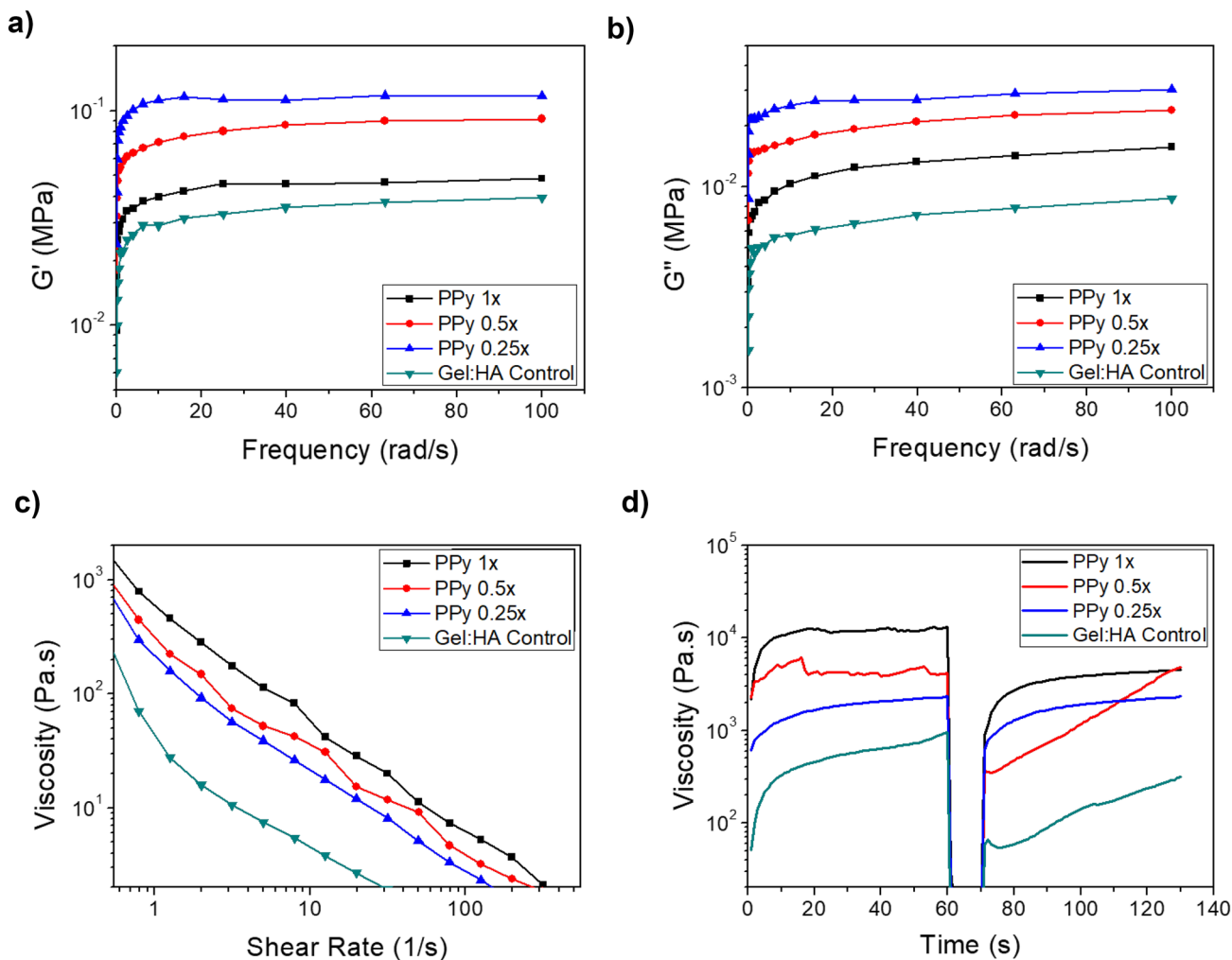


**Fig. 5 a–d** Rheological analysis of Gel:HA:PPy-NP hydrogels at different PPy NP concentrations. **a** Storage modulus as a function of frequency, **b** Loss modulus as a function of frequency. **c** Viscosity

dependent on shear rate. **d** Recovery profile simulating 3D printing with viscosity depended on shear stress

### 3.8 Biocompatibility of Gel:HA:PPy-NP scaffolds

The possible cytotoxic effects of the Gel:HA:PPy-NP materials were initially investigated by means of Alamar Blue™ Proliferation Assay. Mesenchymal stem cells were seeded

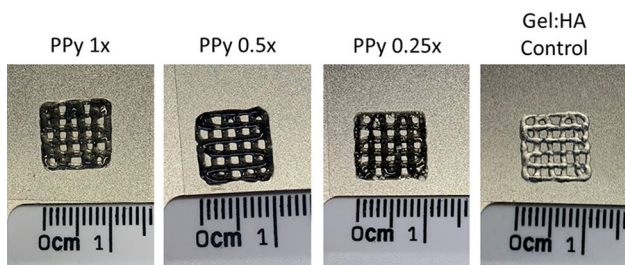


**Fig. 6** 3D printed lattices of Gel:HA:PPy-NP hydrogels before a crosslinking regime is introduced

onto Gel:HA:PPy-NP freeze-dried scaffolds and their proliferation was recorded via fluorescence over a period of 96 h, with results shown in Fig. 7a. The proliferation rates of MSCs followed a similar trend across all samples over the 96 h observational period, with the cells maintaining similar proliferation rates over the observation period. Decreasing the PPy NP concentration did not significantly affect the proliferation rates, for example at the 48 h timepoint the proliferation rate of PPy 1x was  $49 \pm 9\%$  compared to PPy 0.25x at  $49 \pm 13\%$ , though the proliferation rates were lower than the scaffold control i.e. (Gel:HA) with no NPs, as well as the cell control. The latter could be potentially explained as a limitation of the experimental setup. When seeding cells on a scaffold, it is much more difficult to dispense the desired number of cells without any cells washing away during the process when compared to a more precise cell seeding onto a well plate. Therefore, the lower cell seeding

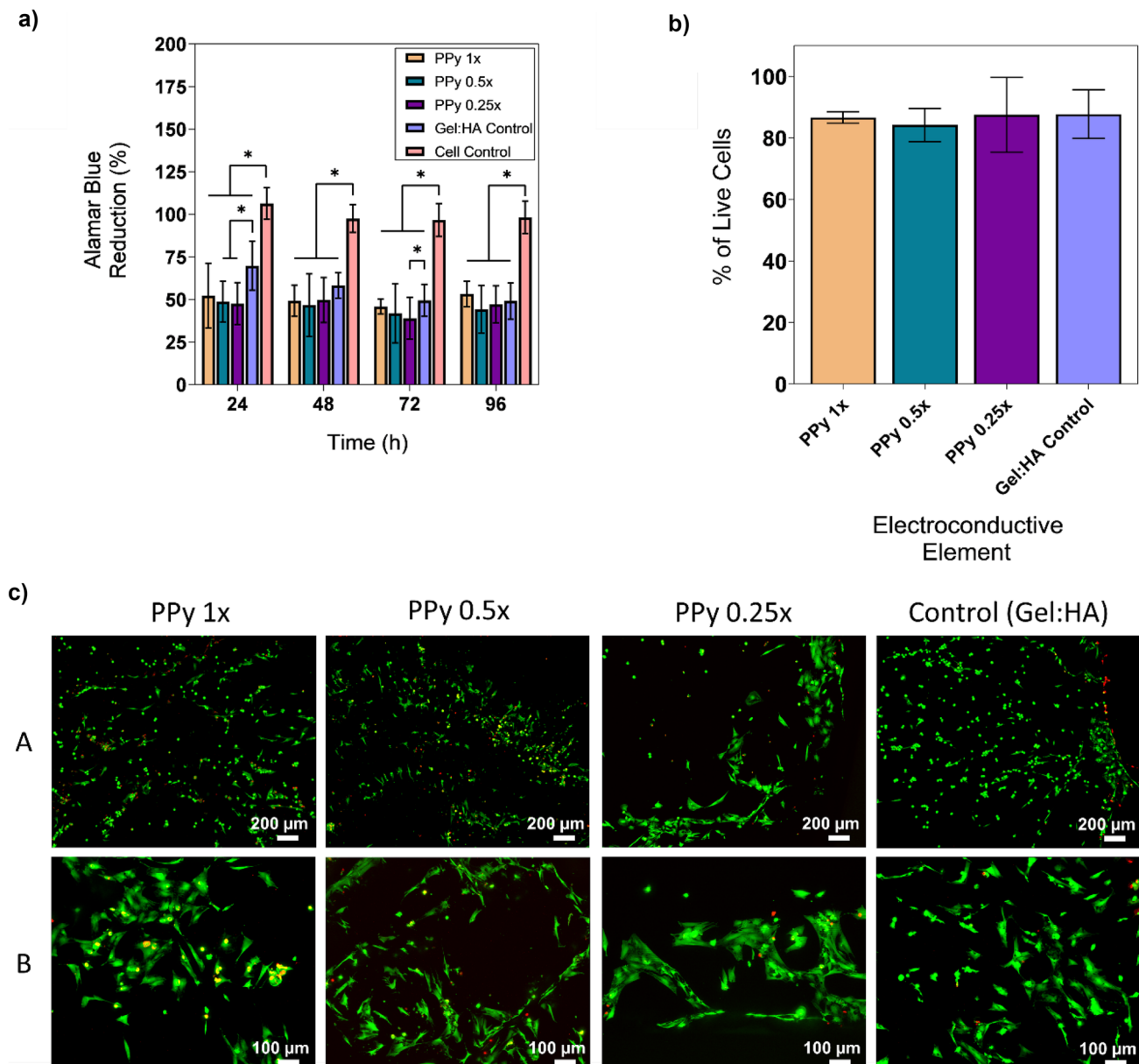


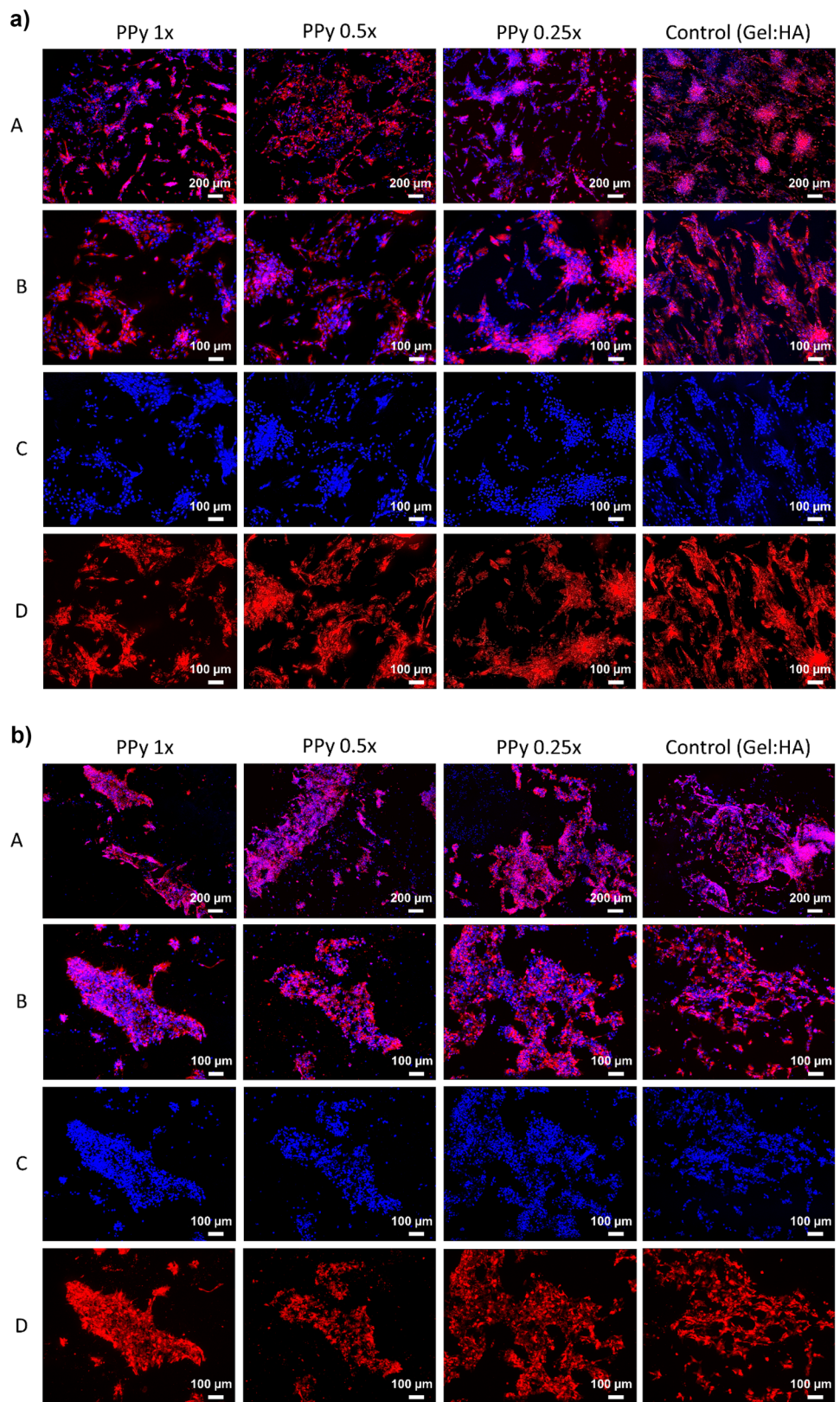
**Fig. 7** MSCs cultured on Gel:HA:PPy-NP scaffolds shows high viability and good cellular morphology when examined in vitro. **a** Cytotoxicity of MSCs measured by means of Alamar Blue™ Proliferation Assay cultured for 96 h in the presence of Gel:HA:PPy-NP scaffolds. **b** Quantification of cellular viability from LIVE/DEAD assay, gath-

ered by means of ImageJ from (c). **c** LIVE/DEAD staining of MSCs seeded on Gel:HA:PPy-NP scaffolds of different PPy NPs concentrations for 96 h. (A) Top scale bar—200  $\mu\text{m}$  (B) Bottom scale bar—100  $\mu\text{m}$ . \* $p < 0.05$  ( $n = 3$ , mean  $\pm$  SD) is indicated where statistical difference is observed

density present on scaffolds may explain the apparently lower proliferation rates than in the cell control. However, the constant proliferation rates over a period of 96 h period strongly indicate that these scaffolds do not illicit a cytotoxic response for MSCs. A two-way ANOVA shows a statistical difference in the proliferation rates of cells between the scaffold groups and the cell control across the 96-h observation period.

Visualisation of MSCs cultured on Gel:HA:PPy-NP scaffolds for 96 h was initially performed utilising a LIVE/DEAD assay, with the results shown in Fig. 7c. Across all groups, high levels of cell viability were detected. The morphology of the cells was also typical of MSCs with spindle-like projections observed [41, 61]. Quantification of the cell viability by ImageJ analysis is presented in Fig. 7b. Across all groups, the percentage of live cells was higher than 84%,

**Fig. 8** MSCs and NSCs cultured on Gel:HA:PPy-NP scaffolds shows good cellular morphology and attachment when examined in vitro. **a** Previously stained with DiI MSCs (red) seeded on Gel:HA:PPy-NP scaffolds of different PPy NPs concentrations for 96 h, fixed with PFA and stained with DAPI (blue). **A** DiI/DAPI scale bar—200  $\mu$ m. **B** DiI/DAPI scale bar—100  $\mu$ m. **C** DAPI scale bar—100  $\mu$ m. **D** DiI scale bar—100  $\mu$ m. **b** Previously stained with TdTomato NSCs (red) seeded on Gel:HA:PPy-NP scaffolds of different PPy NPs concentrations for 96 h, fixed with PFA and stained with DAPI (blue). **A** tdTomato/DAPI scale bar—200  $\mu$ m, **B** tdTomato/DAPI scale bar—100  $\mu$ m, **C** DAPI scale bar—100  $\mu$ m, and **D** tdTomato scale bar—100  $\mu$ m



with the PPy 1 × scaffolds viability at  $87 \pm 2\%$ , which compares favourably with the Gel:HA control at  $88 \pm 8\%$ .

To analyse the cellular attachment of MSCs onto Gel:HA:PPy-NP scaffolds, MSCs which were previously stained with DiI were seeded onto the scaffolds and cultured for a period of 96 h. The cells were then fixed and stained with DAPI for nuclear identification, with the results shown in Fig. 8a. Overall, MSC attachment onto the scaffolds was very prominent, with the cellular arrangement following patterns on the surface of the scaffold. Cells were observed growing in clusters within the grooves and pores of the scaffolds, as shown in the scaffold surface topography in Fig. 2a-A. The morphology of the attached cells also possessed spindle-like projections, in line with normal MSC morphology.

The cellular attachment was also examined using NSCs to investigate the possibility of utilising the scaffolds in neural TE strategies, with tdTomato NSCs seeded and cultured for 96 h on top of Gel:HA:PPy-NP scaffolds and followed by DAPI staining, as shown in Fig. 8b. The attachment of NSCs onto the scaffold of various PPy NP concentrations was successful with cellular projections visible. As in the case of MSCs, the arrangement of NSCs into clusters on top of the scaffolds was primarily determined by the surface topography of the scaffolds.

Successful attachment of the cells onto the Gel:HA:PPy-NP scaffolds was primarily driven by the biomaterial component of gelatin, which possesses GFOGER and RGD peptide sequences which provide cell adhesive ligands for cellular attachment [6, 7, 40]. The successful cell attachment, proliferation and high viability of cells seeded on Gel:HA:PPy-NP scaffolds indicates that the addition of PPy NPs does not elicit cytotoxic effects on cultured cells. Further, the scaffolds are biocompatible when examined in vitro, showcasing their potential use in electroactive TE strategies such as neuronal repair. Further in vitro and particularly in vivo studies are required to elucidate the biological response fully in the presence of these conductive scaffolds.

## 4 Conclusions

Polypyrrole nanoparticles were successfully synthesised using a chemical oxidation polymerization in mini-emulsion technique, which allowed the synthesis of stable and round nanoparticles of  $187 \pm 24$  nm in diameter. These polypyrrole nanoparticles circumvent the limitations associated with polypyrrole polymer in terms of biocompatibility issues. Polypyrrole nanoparticles can be evenly distributed within a scaffold consisting of gelatin and hyaluronic acid (Gel:HA:PPy-NP). The base components of the scaffold were chosen to possess cell attachment

sites and provide anti-inflammatory immunomodulatory cues. Physico-chemical characterisation shows that the Gel:HA:PPy-NP scaffolds possess excellent mechanical properties of  $1.08 \pm 0.26$  MPa and optimal porosity levels. The incorporation of the conductive polypyrrole nanoparticles increased the conductivity of the scaffolds by almost two-fold to  $4.3 \times 10^{-6} \pm 1.1 \times 10^{-6}$  S.cm<sup>-1</sup>. Shear-thinning behaviour, as well as excellent post-printing recovery, highlight that these materials have the potential to be 3D printed into a wide array of geometries and architectures. Biocompatibility studies with mesenchymal stem cells and neuronal stem cells indicate that the Gel:HA:PPy-NP scaffolds are biocompatible with good cell attachment and proliferation profiles. The arrangement of mesenchymal stem cells and neuronal stem cells followed the scaffold surface topography. Taking the results overall, the Gel:HA:PPy-NP materials may be processed both using conventional and advanced manufacturing methods to produce scaffolds that show great promise for the regeneration of electroactive tissues in applications such as neuronal, spinal, and cardiac repair.

**Supplementary Information** The online version contains supplementary material available at <https://doi.org/10.1007/s42114-023-00665-w>.

**Acknowledgements** The authors would like to sincerely thank Dr. Atul K. Garg for the support and mentorship provided throughout the duration of this project, as well as Prof. Mark Tuszynski at the Neuroscience Department at the University of California, San Diego, for the support and technical knowledge during the in vitro studies.

**Author contributions** A.S. and M.C.—data curation. A.S., M.C. and M.N.C.—writing of the manuscript. M.C., M.N.C. and J.K.—supervision. A.S., M.C., A.K.G., J.M.O., J.K and M.N.C.—revision of the manuscript. A.S. and M.N.C.—funding acquisition. The authors read and approved the final manuscript.

**Funding** Open Access funding provided by the IReL Consortium. The authors would like to thank the funding provided by the Irish Research Council through the Irish Research Council Enterprise Partnership Scheme with Johnson and Johnson (EPSPG/2020/78), as well as the Irish Fulbright Commission.

**Data availability** The datasets used and/or analysed during the current study are available from the corresponding author on reasonable request.

## Declarations

**Ethics approval and consent to participate** Not applicable.

**Conflicts of interest** The authors declare no competing interests.

**Open Access** This article is licensed under a Creative Commons Attribution 4.0 International License, which permits use, sharing, adaptation, distribution and reproduction in any medium or format, as long as you give appropriate credit to the original author(s) and the source, provide a link to the Creative Commons licence, and indicate if changes were made. The images or other third party material in this article are

included in the article's Creative Commons licence, unless indicated otherwise in a credit line to the material. If material is not included in the article's Creative Commons licence and your intended use is not permitted by statutory regulation or exceeds the permitted use, you will need to obtain permission directly from the copyright holder. To view a copy of this licence, visit <http://creativecommons.org/licenses/by/4.0/>.

## References

- Kurniawan NA (2019) The ins and outs of engineering functional tissues and organs: evaluating the in-vitro and in-situ processes. *Curr Opin Organ Transplant* 24(5):590–597
- Murphy CA, Collins MN (2018) Microcrystalline cellulose reinforced polylactic acid biocomposite filaments for 3D printing. *Polym Compos* 39(4):1311–1320
- Shkarina S et al (2018) 3D biodegradable scaffolds of polycaprolactone with silicate-containing hydroxyapatite microparticles for bone tissue engineering: high-resolution tomography and in vitro study. *Sci Rep* 8(1):8907
- Carriel V et al (2014) Tissue engineering of the peripheral nervous system. *Expert Rev Neurother* 14(3):301–318
- da Silva D et al (2018) Biocompatibility, biodegradation and excretion of polylactic acid (PLA) in medical implants and theranostic systems. *Chem Eng J* 340:9–14
- Serafin A et al (2021) Printable alginate/gelatin hydrogel reinforced with carbon nanofibers as electrically conductive scaffolds for tissue engineering. *Mater Sci Eng, C* 122
- Davidenko N et al (2016) Evaluation of cell binding to collagen and gelatin: a study of the effect of 2D and 3D architecture and surface chemistry. *J Mater Sci Mater Med* 27(10):148
- Zamboni F et al (2018) The potential of hyaluronic acid in immunoprotection and immunomodulation: chemistry, processing and function. *Prog Mater Sci* 97:97–122
- Misra S et al (2015) Interactions between hyaluronan and its receptors (CD44, RHAMM) regulate the activities of inflammation and cancer. *Front Immunol* 6:201–201
- Collins MN et al (2022) The role of hyaluronic acid in tissue engineering. In: Oliveira JM, Radhouani H, Reis RL (eds) polysaccharides of microbial origin: biomedical applications. Springer International Publishing, Cham, pp 1063–1116
- Huebner EA, Strittmatter SM (2009) Axon regeneration in the peripheral and central nervous systems. *Results Probl Cell Differ* 48:339–351
- Doblado LR, Martínez-Ramos C, Pradas MM (2021) Biomaterials for neural tissue engineering. *Front Nanotechnol* 3
- Serafin A, Rubio MC, Collins MN (2022) Naturally derived biomaterials for spinal cord injury repair. In: Baskar C, Ramakrishna S, Daniela La Rosa A (eds) Encyclopedia of green materials. Springer Nature Singapore, Singapore, pp 1–10
- Collins MN et al (2022) Emerging scaffold- and cellular-based strategies for brain tissue regeneration and imaging. *In vitro models* 1(2):129–150
- Khaing ZZ et al (2011) High molecular weight hyaluronic acid limits astrocyte activation and scar formation after spinal cord injury. *J Neural Eng* 8(4)
- Litwiniuk M et al (2016) Hyaluronic Acid in Inflammation and Tissue Regeneration. *Wounds* 28(3):78–88
- Ni J et al (2022) Resistance to aggregation-caused quenching: chitosan-based solid carbon dots for white light-emitting diode and 3D printing. *Adv Compos Hybrid Mater* 5(3):1865–1875
- Pan P et al (2022) Biologically enhanced 3D printed micro-nano hybrid scaffolds doped with abalone shell for bone regeneration. *Adv Compos Hybrid Mater* 6(1):10
- Amrita A et al (2022) Biodegradable filament for 3D printing process: a review. *Eng Sci* 18:11–19
- Yang J et al (2022) High-precision three-dimensional printing in a flexible, low-cost and versatile way: a review. *ES Mater Manuf* 15:1–13
- Xia X et al (2020) Microalgal-immobilized Biocomposite Scaffold Fabricated by Fused Deposition modeling 3D printing technology for dyes removal. *ES Mater Manuf* 7:40–50
- Zhao Y et al (2022) Direct ink printing reduced graphene oxide/KCu7S4 electrodes for high-performance supercapacitors. *Adv Compos Hybrid Mater* 5(2):1516–1526
- Zhao Y et al (2022) Three-dimensional printing of the copper sulfate hybrid composites for supercapacitor electrodes with ultra-high areal and volumetric capacitances. *Adv Compos Hybrid Mater* 5(2):1537–1547
- Wang X et al (2023) Direct 3D printing of piezoelectrets: process feasibility, prototypes fabrication and device performance. *Eng Sci* 21:800
- Steel EM, Azar J-Y, Sundararaghavan HG (2020) Electrospun hyaluronic acid-carbon nanotube nanofibers for neural engineering. *Materialia* 9
- Chen MQ et al (2008) Cardiac differentiation of embryonic stem cells with point-source electrical stimulation. *Annu Int Conf IEEE Eng Med Biol Soc* 2008:1729–1732
- Banan Sadeghian R, Ebrahimi M, Salehi S (2018) Electrical stimulation of microengineered skeletal muscle tissue: effect of stimulus parameters on myotube contractility and maturation. *J Tissue Eng Regen Med* 12(4):912–922
- Fu C et al (2019) Effect of electrical stimulation combined with graphene-oxide-based membranes on neural stem cell proliferation and differentiation. *Artificial Cells, Nanomedicine, and Biotechnology* 47(1):1867–1876
- Fan L et al (2017) Polyaniline promotes peripheral nerve regeneration by enhancement of the brain-derived neurotrophic factor and ciliary neurotrophic factor expression and activation of the ERK1/2/MAPK signaling pathway. *Mol Med Rep* 16(5):7534–7540
- Abedi A, Hasanzadeh M, Tayebi L (2019) Conductive nanofibrous Chitosan/PEDOT:PSS tissue engineering scaffolds. *Mater Chem Phys* 237
- Saleemi MA et al (2021) Toxicity of carbon nanotubes: molecular mechanisms, signaling cascades, and remedies in biomedical applications. *Chem Res Toxicol* 34(1):24–46
- Mantione D et al (2017) Poly(3,4-ethylenedioxythiophene) (PEDOT) Derivatives: innovative conductive polymers for bioelectronics. *Polymers* 9(8):354
- Song E, Choi J-W (2013) Conducting Polyaniline Nanowire and Its Applications in Chemiresistive Sensing. *Nanomaterials (Basel, Switzerland)* 3(3):498–523
- Liang S et al (2018) Paintable and rapidly bondable conductive hydrogels as therapeutic cardiac patches. *Adv Mater* 30(23):1704235
- Zhou L et al (2018) Soft conducting polymer hydrogels cross-linked and doped by tannic acid for spinal cord injury repair. *ACS Nano* 12(11):10957–10967
- Arakawa CK, DeForest CA (2017) Chapter 19 - polymer design and development. In: Vishwakarma A, Karp JM (eds) biology and engineering of stem cell niches. Academic Press, Boston, pp 295–314
- Meng S et al (2008) Heparin dopant increases the electrical stability, cell adhesion, and growth of conducting polypyrrole/poly(L, L-lactide) composites. *J Biomed Mater Res A* 87(2):332–344
- Zhou L et al (2020) Biodegradable conductive multifunctional branched poly(glycerol-amino acid)-based scaffolds for tumor/infection-impaired skin multimodal therapy. *Biomaterials* 262

39. Wu C et al (2019) Cell-laden electroconductive hydrogel simulating nerve matrix to deliver electrical cues and promote neurogenesis. *ACS Appl Mater Interfaces* 11(25):22152–22163
40. Serafin A, Culebras M, Collins MN (2023) Synthesis and evaluation of alginate, gelatin, and hyaluronic acid hybrid hydrogels for tissue engineering applications. *Int J Biol Macromol* 123438
41. Serafin A et al (2022) Electroconductive PEDOT nanoparticle integrated scaffolds for spinal cord tissue repair. *Biomaterials Res* 26(1):63
42. Pawelec KM et al (2014) A design protocol for tailoring ice-templated scaffold structure. *J R Soc Interface* 11(92):20130958–20130958
43. Azimi Yancheshme A, Momen G, Jafari Aminabadi R (2020) Mechanisms of ice formation and propagation on superhydrophobic surfaces: a review. *Adv Colloid Interf Sci* 279:102155
44. Xu K et al (2018) Influence of hydrophobicity on ice accumulation process under sleet and wind conditions. *AIP Adv* 8(3)
45. Murphy CM, O'Brien FJ (2010) Understanding the effect of mean pore size on cell activity in collagen-glycosaminoglycan scaffolds. *Cell Adh Migr* 4(3):377–381
46. Bilston LE, Thibault LE (1996) The mechanical properties of the human cervical spinal cord in vitro. *Ann Biomed Eng* 24(1):67–74
47. Oakland RJ et al (2006) The biomechanical response of spinal cord tissue to uniaxial loading. *Proc Inst Mech Eng H* 220(4):489–492
48. Bagher Z et al (2019) Conductive hydrogel based on chitosan-aniline pentamer/gelatin/agarose significantly promoted motor neuron-like cells differentiation of human olfactory ecto-mesenchymal stem cells. *Mater Sci Eng, C* 101:243–253
49. Sikorski P (2020) Electroconductive scaffolds for tissue engineering applications. *Biomaterials Science* 8(20):5583–5588
50. Mevold AHH et al (2015) Fabrication of gold nanoparticles/graphene-PDDA nanohybrids for bio-detection by SERS nanotechnology. *Nanoscale Res Lett* 10(1):397
51. Sungoradee T, Srikulkit K (2022) Preparation and characterizations of PSS/PDADMAC polyelectrolyte complex hydrogel. *Polymers* 14(9):1699
52. Qiao C, Cao X (2014) Swelling behavior of physically cross-linked gelatin gels in varied salt solutions. *J Macromol Sci Part B* 53(10):1609–1620
53. Skopinska-Wisniewska J, Tuszyńska M, Olewnik-Kruszkowska E (2021) Comparative study of gelatin hydrogels modified by various cross-linking agents. *Materials (Basel, Switzerland)* 14(2):396
54. Kuijpers AJ et al (2000) Cross-linking and characterisation of gelatin matrices for biomedical applications. *J Biomater Sci Polym Ed* 11(3):225–243
55. Sujan MI et al (2020) Bi-functional silica nanoparticles for simultaneous enhancement of mechanical strength and swelling capacity of hydrogels. *RSC Adv* 10(11):6213–6222
56. Saarai A et al (2013) On the development and characterisation of crosslinked sodium alginate/gelatin hydrogels. *J Mech Behav Biomed Mater* 18:152–166
57. Yussuf A et al (2018) Synthesis and characterization of conductive polypyrrole: the influence of the oxidants and monomer on the electrical, thermal, and morphological properties. *Int J Polym Sci* 2018:4191747
58. Khadem F et al (2017) Morphology control of conducting polypyrrole nanostructures via operational conditions in the emulsion polymerization. *J Appl Polym Sci* 134(15)
59. Li H, Liu S, Lin L (2016) Rheological study on 3D printability of alginate hydrogel and effect of graphene oxide. *Int J Bioprinting* 2(2)
60. Gillispie G et al (2020) Assessment methodologies for extrusion-based bioink printability. *Biofabrication* 12(2)
61. Haasters F et al (2009) Morphological and immunocytochemical characteristics indicate the yield of early progenitors and represent a quality control for human mesenchymal stem cell culturing. *J Anat* 214(5):759–767

**Publisher's Note** Springer Nature remains neutral with regard to jurisdictional claims in published maps and institutional affiliations.